AIAA SciTech Forum
23-27 January 2023, National Harbor, MD & Online
AIAA SCITECH 2023 Forum

10.2514/6.2023-0539

Microstructure-Sensitive Materials Design with Physics-Informed Neural Networks

Mahmudul Hasan *, Zekeriya Ender Eger†, Arulmurugan Senthilnathan‡, and Pınar Acar§
Virginia Tech, Blacksburg, VA-24061

Microstructure-sensitive material design has become popular among materials engineering researchers in the last decade because it allows the control of material performance through the design of microstructures. In this study, the microstructure is defined by an orientation distribution function (ODF). A physics-informed machine learning approach is integrated into microstructure design to improve the accuracy, computational efficiency, and explainability of microstructure-sensitive design. When data generation is costly and numerical models need to follow certain physical laws, machine learning models that are domain-aware perform more efficiently than conventional machine learning models. Therefore, a new paradigm called Physics-Informed Neural Network (PINN) is introduced in the literature. This study applies the PINN to microstructure-sensitive modeling and inverse design to explore the material behavior under deformation processing. In particular, we demonstrate the application of PINN to small-data problems driven by a crystal plasticity model that needs to satisfy the physics-based design constraints of the microstructural orientation space. For the first problem, we predict the microstructural texture evolution of Copper during a tensile deformation process as a function of initial texturing and strain rate. The second problem aims to calibrate the crystal plasticity parameters of Ti-7Al alloy by solving an inverse design problem to match PINN-predicted final texture prediction and the experimental data.

Nomenclature

$\mathbf{A}$	=	orientation distribution function (ODF)
$\mathbf{b}$	=	bias of the network
h^{β}	=	single slip hardening rate
J	=	total loss
$\mathbf{L}$	=	velocity gradient
$LSTM$	=	long short-term memory
$\mathbf{p}$	=	property matrix
$PINN$	=	physics-informed neural network
$\mathbf{q}$	=	volume normalization vector
q	=	latent hardening rate
$\mathbf{R}$	=	lattice rotation
$RMSE$	=	root mean squared error
$\mathbf{W}$	=	weight matrix
Y	=	ODF output by physics-based simulator
$\hat{Y}$	=	predicted ODF by PINN

I. Introduction

Research on multi-scale materials modeling is focused on examining the connection between thermo-mechanical processes, structures, and material characteristics by investigating physical behavior at multiple length and time

*Graduate Research Assistant, Ph.D. Student, Department of Mechanical Engineering, AIAA Student Member
†Graduate Research Assistant, Ph.D. Student, Department of Mechanical Engineering
‡Graduate Research Assistant, Ph.D. Student, Department of Mechanical Engineering, AIAA Student Member
§Assistant Professor, Department of Mechanical Engineering, AIAA Member

scales. Understanding the multi-scale material response by utilizing entirely experimental approaches is infeasible due to the overwhelming amount of parameters/conditions that must be investigated [1]. Therefore, computational approaches are required to assess the multi-scale characteristics and performance of materials. The multi-scale computational efforts have been increasingly visible since the introduction of the Integrated Computational Materials Science (ICME) paradigm [2]. The ICME paradigm, in particular, supports the application of next-generation numerical methodologies in order to improve the current understanding of materials modeling and design. To achieve this goal, we build novel physics-informed and data-driven crystal plasticity surrogate models of processing-microstructure-property linkages for two metallic materials using long short-term memory (LSTM) network.

Extracting useful information from existing data through various computing resources has become an important paradigm in different scientific disciplines including image recognition, cognitive science, and genomics [3]. Like other fields, machine learning (ML) has also become a popular approach for materials design and discovery [4]. In the past, data-driven ML has been applied to different studies in the field, including the polycrystalline material design [5, 6], material discovery [7, 8], and microstructure design for obtaining specific design parameters [9, 10]. For instance, an ML-based crystal plasticity model representation for Titanium-7wt%Aluminum (Ti-7Al) alloy was developed by Acar [11] using data-driven supervised learning techniques. While these data-driven predictive ML models are widely utilized, their prediction accuracy is immediately related to the quality and size of the training data.

Many engineering models are built upon underlying physics. The solutions of these physics-based models also need to satisfy boundary conditions, initial conditions, and physics-derived design constraints. For traditional data-driven modeling, a large amount of data are required to build a high-fidelity model [12]. However, due to computational time requirements, it is not efficient for some models like crystal plasticity modeling to produce sufficient data to train a high-fidelity ML model. Moreover, traditional ML models may not be *explainable* as they may not be aware of the underlying physics-based design constraints [13]. To incorporate the problem physics within the ML model and train the model with small data, a new framework called Physics-Informed Neural Network (PINN) was introduced by Raissi et al. [3]. Before this study, Lee et al. [14] first applied a neural network algorithm to solve the differential equations. After that, Lagaris et al. [15] solved ordinary and partial differential equations using artificial neural networks. They used a similar methodology to solve boundary value problems with irregular boundaries [16]. Later, Sirignano et al. [17] developed a deep learning algorithm to solve high-dimensional (up to 200 dimensions) partial differential equations (PDEs) with boundary and initial conditions. PINN has become very popular within the scientific community since Raissi et al. published a detailed framework of PINN for solving PDEs [18] and discovery of PDEs [19]. Later, they published an integrated version of the previous two articles [3]. Subsequently, PINN was adopted in different engineering applications, such as solid mechanics [20–22], crystal plasticity modeling [23, 24], fluid mechanics [25–29], heat transfer [30], nano-optics, metamaterials [31, 32], medicine [33–35], and power systems [36]. Recently, PINN was also applied to quantify the model uncertainty [37–39].

In order to optimize the processing paths (up to 100 combinations) for a targeted metallic microstructure, Dornheim et al. [40] recently formulated a model-free deep reinforcement learning algorithm. Instead of relying on prior samples, their algorithm can communicate with processing simulations during optimization. They expanded the technique to address multi-objective optimization problems. In a different study, Honarmandi et al. [41] proposed a novel approach based on batch Bayesian optimization to solve the inverse problem of determining the material processing requirements using microstructure data. They created a surrogate model based on Gaussian process regression to take the place of the computationally expensive process models and integrated it into inverse design optimization using both low-fidelity and high-fidelity phase field models. In this study, inspired by PINN, we develop physics-informed and data-driven surrogate models to replace costly material processing simulations to predict the final deformed textures and their evolutions over time. Models are trained with small data and customized to incorporate the underlying physics-derived constraints. Therefore, this article presents a combined approach of microstructure-sensitive materials design and physics-informed ML. The example problems will be presented for two different crystal structures, i.e., hexagonal close-packed (hcp) and cubic. Two example materials, Ti-7Al and Copper (Cu), are chosen as they have wide engineering applications under high thermo-mechanical stresses, including aerospace systems. In the first problem, we develop a surrogate model for Cu, which predicts the final texture and its evolution at different time steps when a tensile force is applied to the material for a certain time with different strain rates. Next, we define an inverse design problem to solve the optimum slip and twin system parameters of Ti-7Al to achieve a final texture prediction that matches the experimental texture data. In order to do that, another surrogate model is developed to predict the deformed texture as a function of crystal plasticity parameters when the material is under compression. In both cases, long short-term memory (LSTM) neural network is implemented to develop a data-driven ML model. LSTM network is a good choice because our study involves time-dependent simulation data. Moreover, the physics-based constraints can be implemented in the LSTM

network [42–45]. The organization of this article is as follows: Section II describes the mathematical modeling of the deformation processing and texture evolution. It also discusses the necessary mathematical background of the physics-informed LSTM network. Results for forward modeling and inverse design using PINN are discussed in Section III. The summary of the article along with potential future works is included in Section IV.

II. Mathematical Modeling

A. Deformation Process and Texture Evolution Modeling

The Orientation Distribution Function (ODF) approach is used to represent the microstructural texture using a local finite element discretization scheme. The ODF is a probabilistic one-point descriptor that quantifies microstructural texture in terms of volume fractions of individual crystal orientations. A polycrystalline material is made up of many crystals, each of which has its unique crystallographic orientation. The ODFs can be updated as a function of time using a crystal plasticity constitutive model, making it a computationally efficient method. The probabilities are developed specifically from time $t = 0$, which corresponds to an initial ODF derived from the initial microstructural texture. Rodrigues' axis-angle parameterization of the orientation space approach is applied to depict ODFs [46]. The parameterization is obtained from the scaling of the axis of rotation, n, which is represented as: $n = r/tan(\theta/2)$ where r and θ are the orientation and angle of rotation, respectively. The ODF is represented by $\mathbf{A}(r, t)$. To calculate the meso-scale (homogenized) characteristics, a local finite element discretization approach is used along with Rodrigues' parametrization. The definition of the ODF, in terms of the volume densities of the crystals, requires the implementation of the normalization constraint that is expressed as in Eq. 1:

$$\int \mathbf{A}(r,t)\, dr = 1 \tag{1}$$

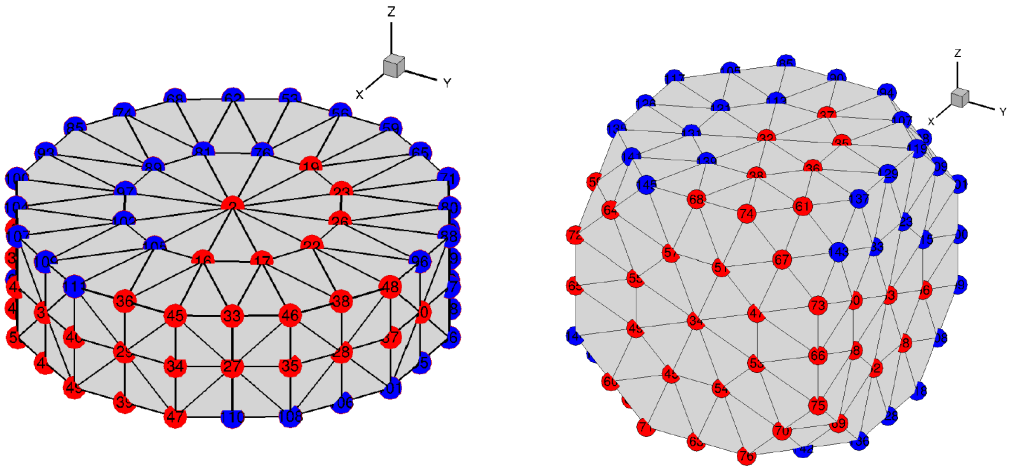

(a) (b)

Fig. 1 Finite element discretization of the orientation space for (a) hexagonal close-packed (HCP) and (b) cubic microstructures. The red-colored nodal points show the independent ODF values while the blue-colored nodes indicate the dependent ODFs as a result of the crystallographic symmetries.

The discretization of the ODF is shown in Fig. 1, which contains N independent nodes with N_{elem} finite elements and N_{int} integration points per element. Figure 1(a) represents the hexagonal microstructure and Fig. 1(b) depicts the cubic microstructure. The number of independent nodal points (the nodes shown with red color in Fig. 1) of an HCP microstructure is 50 with the Rodrigues representation while the number of independent ODFs is 76 for the cubic microstructure. Using a local finite element discretization scheme in the Rodrigues fundamental region, two equations are derived to compute the volume-averaged material properties in terms of the ODF values. These two equations are given below:

$$\mathbf{q}^{\mathbf{T}}\mathbf{A} = 1 \tag{2}$$

$$< \chi >= \mathbf{p^T A} \tag{3}$$

Equation 2 is derived from Eq. 1 where **q** is the volume normalization vector, which is a function of the finite element discretization terms and the Rodrigues orientation space metric. In Eq. 3, **p** is the single crystal property matrix that is used to compute the volume-averaged and orientation-dependent material property, $< \chi >$.

The texture of a polycrystalline microstructure changes under applied loads during a deformation process. This change is reflected in the ODF values through the ODF conservation equation [47], which is given below.

$$\frac{\partial A(\mathbf{r},t)}{\partial t} + \nabla A(\mathbf{r},t) \cdot v(\mathbf{r},t) + A(\mathbf{r},t)\nabla \cdot v(\mathbf{r},t) = 0 \tag{4}$$

Equation 4 also satisfies the volume normalization constraint of Eq. 2 at a given time. Here, the ODF, **A**, is a function of crystallographic orientations (**r**) and time (t), and $v(\mathbf{r},t)$ is the reorientation velocity. The microstructure constitutive model can calculate texture evolution in terms of a velocity gradient (**L**) definition (see Eq. 5 below), which is linked to $v(\mathbf{r},t)$ by the Taylor macro-micro linking hypothesis. A rate-independent constitutive model is adopted to compute the reorientation velocity [47]. The evolution of current texture $A(\mathbf{r},t)$ from the initial texture $A(\mathbf{r},0)$ is solved by the constitutive model and finite element representation in the Rodrigues orientation space.

Each deformation process, such as tension/compression and shear, generates a particular ODF as output after applying a load for a specific amount of time. The macro velocity gradient, **L**, for a particular process is used by the crystal plasticity solver to explore the ODF evolution during that process. The velocity gradient of a crystal with the orientation, **r**, can be written as:

$$\mathbf{L} = S + \mathbf{R}\sum_{\alpha} \dot{\gamma^{\alpha}} \bar{\mathbf{T}}^{\alpha} \mathbf{R}^T, \tag{5}$$

where S represents the lattice spin, **R** indicates the lattice rotation, $\dot{\gamma^{\alpha}}$ and $\bar{\mathbf{T}}^{\alpha}$ indicate the shearing rate and Schmid tensor for the slip system α, respectively. The macro velocity gradient expression of Eq. 5 can be written in the following matrix form for the tension/compression process (Eq. 6) and its derivation is skipped here for brevity which can be found in Ref. [47].

$$\mathbf{L} = \alpha_1 \begin{bmatrix} 1 & 0 & 0 \\ 0 & -0.5 & 0 \\ 0 & 0 & -0.5 \end{bmatrix} \tag{6}$$

where α_1 relates to the strain rate of the tension/compression process.

Additionally, the slip hardening model is integrated into the crystal plasticity simulations as explained next:

$$h^{\alpha\beta} = [q + (1-q)\delta^{\alpha\beta}]h^{\beta} \quad \text{(no sum on } \beta) \tag{7}$$

where h^{β} is a single slip hardening rate, q is the latent-hardening ratio (which is equal to 1.4 for non-coplanar slip systems), and $\delta^{\alpha\beta}$ is the Kronecker delta function. For the single-slip hardening rate, the following specific form is used:

$$h^{\beta} = h_o(1 - \frac{s^{\beta}}{s_s})^a \tag{8}$$

where h_o, a, and s_s are slip hardening parameters. While the cubic microstructures of Cu only involve 12 slip planes, the HCP Ti-7Al demonstrates a more complex deformation behavior. Accordingly, the basal $< a >$, prismatic $< a >$, pyramidal $< a >$ and pyramidal $< c + a >$ slip systems, in addition to the $\{10\bar{1}2\} < \bar{1}011 >$ twinning mechanism are modeled for Ti-7Al alloy.

B. Physics-Informed Neural Networks

Neural networks are used to estimate the outcomes of a function, therefore, they can be embedded into the physical systems to approximate the solution while satisfying any initial or boundary conditions and physics-derived constraints. In the case of PINNs, the loss function is modified to accommodate the physical laws, initial/boundary conditions, or any design constraints present in the system.

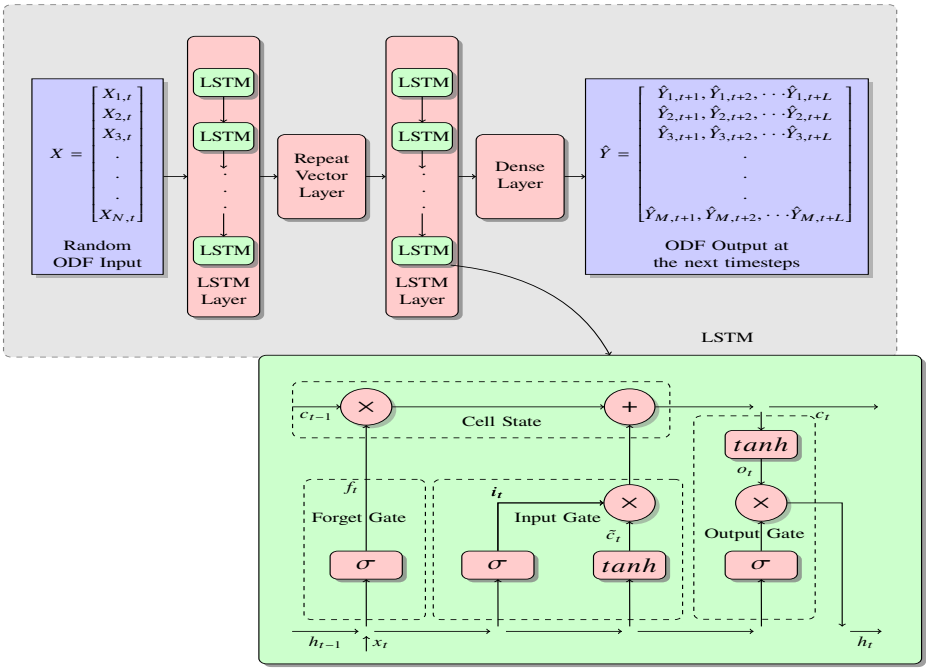

Fig. 2 LSTM architecture adaptation for a multiple parallel time-series problem to predict the evolution of ODFs and internal block structure of an LSTM cell.

Feed Forward Neural Networks (FNN) are the most basic network structure comprised of different layers with many nodes, which map inputs to the outputs by adding weighted inputs with bias. As FNN relays information in only one direction, problems containing parallel time series data that are related to each other, cannot be predicted accurately with this type of network. Therefore, we are utilizing a special type of recurrent neural network (RNN) called long short-term memory (LSTM) network to correlate the processing parameters and texture evolutions with time during the deformation process.

1. Long Short-Term Memory (LSTM) Network

Unlike FNN, RNN has nodes in its layers that communicate with the nodes of the previous layer and also create a cycle, where it can act as a memory to fit the variable sequence inputs. This is achieved by backpropagation, ensuring that the weights in the previous layers are updated based on the derivative of the estimated error at the output layer, with respect to the weights, within a training epoch. As the inputs are not independent of each other, relations between the features could be captured directly. It is also able to handle inputs and outputs of different sizes. However, there are still major issues when implementing the network standalone, such as gradient exploding or vanishing and processing large sequences.

In order to tackle the disadvantages of the RNN structure, LSTM is proposed. The main additions are the gates in the form of activation functions that provide the ability to select which information to discard or to keep in the memory. As summarized in Fig. 2, the cell is composed of a group of neural networks that operates with three gates. The input gate decides whether new information should enter the cell, the forget gate releases the information that is considered not important, and the output gate decides if the whole process starting from the input gate should affect the output. These gates also reduce the time consumed in the training, thus helping the whole neural network system to handle a long sequence effectively. Equations from 9 to 12 give the expressions at the forget, input, and output gates respectively, where $\boldsymbol{W}$ is the gate weight matrix, $\boldsymbol{U}$ corresponds to the hidden unit weight matrix, and $\mathbf{b}$ stands for the bias. After the input x_t and the hidden state h_t are multiplied with the weights, they become inputs for their respective activation functions.

$$f_t = \sigma\left(\boldsymbol{W}^{(f)}\boldsymbol{x}_t + \boldsymbol{U}^{(f)}\boldsymbol{h}_{t-1} + \boldsymbol{b}^{(f)}\right) \tag{9}$$

$$i_t = \sigma\left(\boldsymbol{W}^{(i)} x_t + U^{(i)} h_{t-1} + b^{(i)}\right) \tag{10}$$

$$o_t = \sigma\left(W^{(o)} x_t + U^{(o)} h_{t-1} + b^{(o)}\right) \tag{11}$$

$$g_t = \tilde{C}_t = \tanh\left(W^{(g)} x_t + U^{(g)} h_{t-1} + b^{(g)}\right) \tag{12}$$

These gates are then used to calculate the new memory and the cell output in Equations 13 and 14, respectively [48], with element-wise multiplication, to ensure that gate values either destroys the corresponding value when they are close to zero or allows them to pass when they are close to one.

$$\boldsymbol{C}_t = g_t \bigodot i_t + f_t \bigodot C_{t-1} \tag{13}$$

$$h_t = o_t \bigodot \tanh\left(C_t\right) \tag{14}$$

For modeling the evolution of the Cu microstructure during a tensile process, the first LSTM layer takes the initial ODFs as the input with the addition of the strain rate. The output of the layer is then converted to a multi-column shape for it to conform to the shape of the output that has multiple time steps. For the second problem that explores the optimum crystal plasticity parameters of Ti-7Al alloy to match the final texture data, the first LSTM layer inputs the slip and twin system parameters. The second LSTM layer takes the output of the previous layer and predicts the output through the dense layer. The predicted output $\hat{Y}$ for each time step, based on the strain rate and the initial ODF, is evaluated via a loss function where it is compared with the actual ODF (Y) for the corresponding time step obtained from the physics-based simulator. The loss function is modified to incorporate the physics-based normalization constraint (see Eq. 2) which needs to be satisfied by the ODFs at each time step. Therefore, we have added an extra term in the loss function that accounts for the physics-informed loss which becomes as Total Loss = Physics-Informed Loss + Data-Driven Loss. The total loss (J) can be expressed as:

$$J = \sum_{i=1}^{L}[(1 - q \cdot \hat{Y}_i)^2 + \frac{1}{M}\sum_{j=1}^{M}\left(Y_{i,j} - \hat{Y}_{i,j}\right)^2] \tag{15}$$

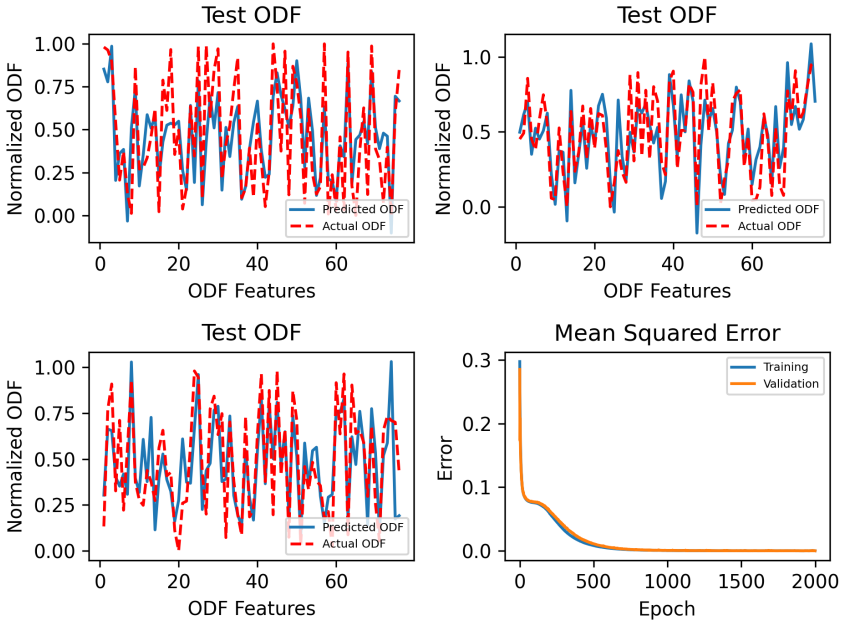

Fig. 3 Comparison of the actual and predicted normalized ODFs for three different test cases along with the convergence of mean squared error for both training and validation data.

Here, the first term ensures that the accuracy search does not violate the physics-based constraint and the second term ensures the minimum error in model prediction.

III. Results and Discussions

Employing the above-mentioned mathematical models, we develop two surrogate models for forward modeling and inverse design of deformation processing. In the forward model, the physics-informed ML model predicts the texture evolution during a tensile deformation process for Cu. In the other problem, we build another surrogate model to predict the final deformed texture as a function of slip and twin system parameters of Ti-7Al. In both cases, training data are generated using the physics-based crystal plasticity simulations with the constitutive model developed by Sundararaghavan et al. [49].

A. Forward Model of Crystal Plasticity Simulations

The objective of this surrogate model is to predict the texture evolution and the final texture of tensile deformation using any given initial texture and strain rate. Copper is considered as the example material that has 76 independent ODFs. We generated 1200 random training data samples of initial textures using the physics-based simulations with strain rates varying from 0.1 to 1 s^{-1}. The tensile force is applied for 0.1 sec in each case. Training data contains the final deformed texture with 9 intermediate time steps of textures in terms of ODF snapshots. 200 data samples are reserved for testing the performance of the model. Among 1000 data samples, 85% and 15% of the data are used for

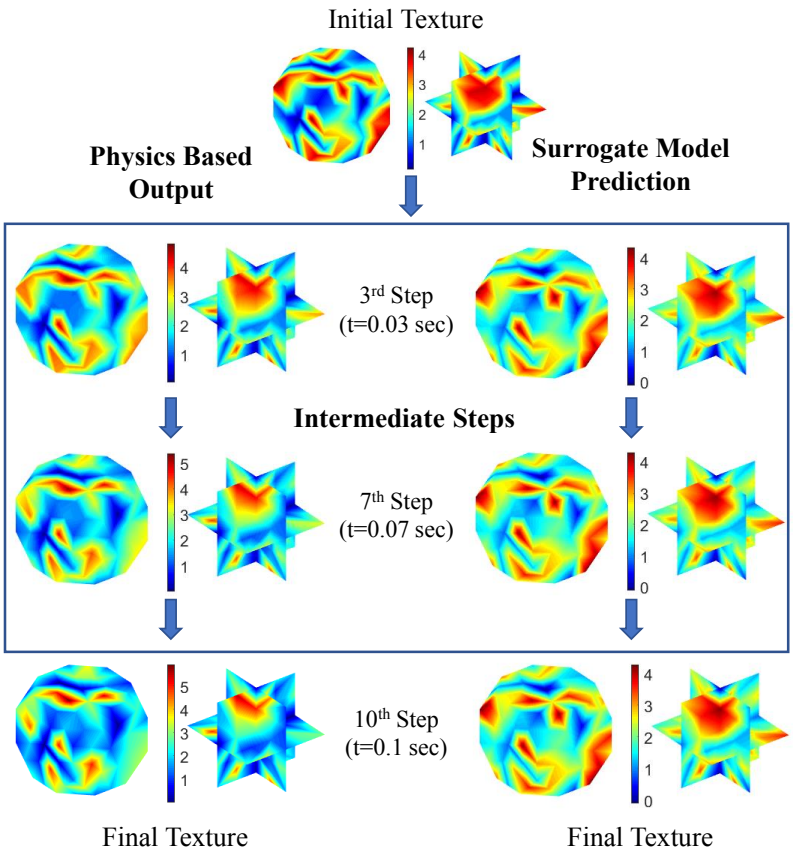

Fig. 4 Comparison of the ODFs in Rodrigues orientation space at different time steps obtained by physics-based model and physics-informed ML model.

Table 1 Optimum ranges for the crystal plasticity parameters for compression [13, 51]

Slip System	s_0 (MPa)	h_0 (MPa)	s_s (MPa)	a
Basal $< a >$	[200, 349.95]	[200, 299.5]	[1500, 1784.2]	[1.3, 2.0149]
Prismatic $< a >$	[220, 399.33]	[200, 299.5]	[1500, 1784.2]	[1.3, 2.0149]
Pyramidal $< a >$	[900, 1199.7]	[200, 299.5]	[1500, 1784.2]	[1.3, 2.0149]
Pyramidal $< c + a >$	[800.2, 1199.1]	[200, 299.5]	[1500, 1784.2]	[1.3, 2.0149]
Twinning	[609.88, 999.28]	[800.12, 1110]	[1500, 1784.2]	[3.6584, 3.9998]

training and validation, respectively. Adam optimizer [50] is used for the training that had 2000 epochs with a batch size of 77 and a learning rate of 0.0001. The trained model is then used to test different sets of ODFs. An example prediction for a set of normalized final ODFs is given in Fig. 3 that shows a high-accuracy match with most of the test points. The root mean squared error (RMSE) values of the predictions are 0.19, 0.16 and 0.21, respectively. In addition, the training and validation accuracy of the model is also reported in Fig. 3.

Furthermore, a random initial texture is chosen to run the process simulation using both physics-based and surrogate models for the strain rate of 1 s^{-1}. The final texture and two intermediate steps of ODF evolution from both models are shown for comparison in Fig. 4. It is evident from Fig. 4 that the physics-informed surrogate model is able to capture the trend of ODF evolution in time with a minimum error (RMSE values are 0.44, 0.65, and 0.85 for 3^{rd}, 7^{th}, and 10^{th} steps, respectively). Moreover, the predicted ODFs in each step satisfy the volume normalization constraint of Eq. 2. It is observed that the RMSE value of the prediction is increasing with time. In addition, these values are higher for predicting the high strain rate processes. The possible reason behind this finding is that larger changes occur in the ODF values from the initial time step to the final time step when the strain rate is high. In such cases, the surrogate model needs more data from the physics-based simulations to achieve high prediction accuracy.

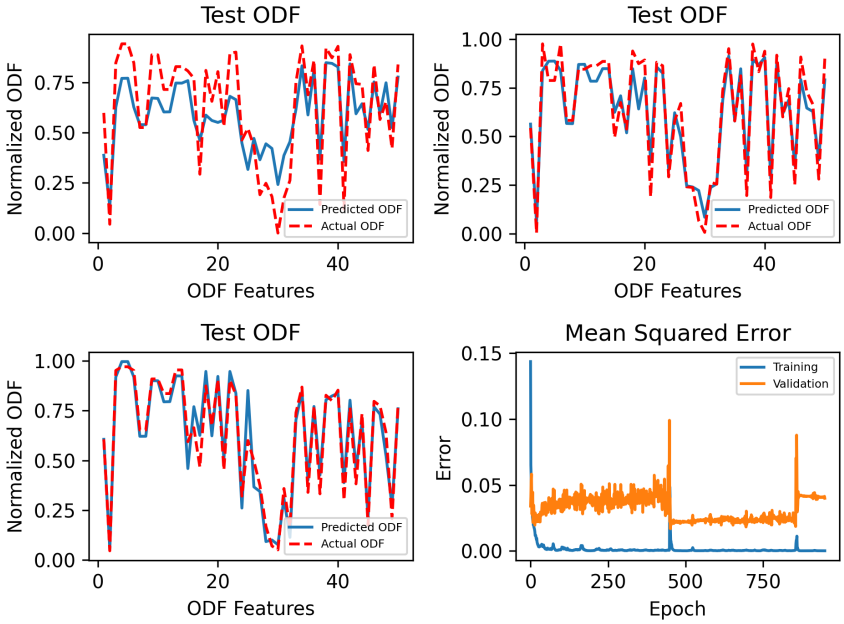

Fig. 5 Comparison of the actual and predicted normalized ODFs for three different test cases along with the convergence of mean squared error for both training and validation data.

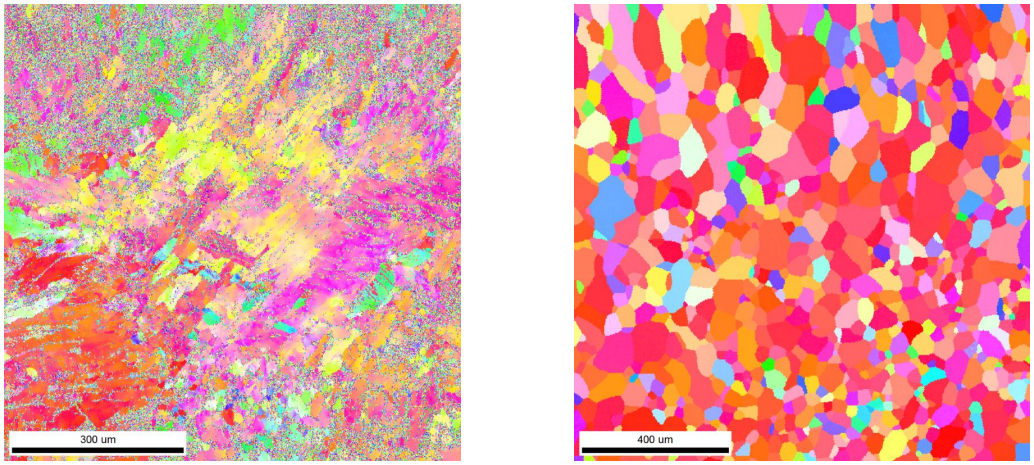

(a) (b)

Fig. 6 Experimental EBSD image of the Ti-7Al alloy sample at 13.5% compressive strain (a) after compression (b) after re-crystallization [53].

B. Inverse Design of Crystal Plasticity Parameters

In our previous study [13], a high-fidelity crystal plasticity surrogate model was developed for Ti-7Al using conventional neural networks. A two-step solution was proposed to develop an inverse problem that yielded optimum crystal plasticity parameters by minimizing the difference between experimental microstructure data and the neural network predictions of the same. However, only 50 data points were generated using PRISMS-Plasticity software [52] to train the model as the data generation was costly. Moreover, the design variables (ODFs) were required to satisfy the normalization constraints. As a result, the overall prediction quality of the conventional neural network was lower than desired. Therefore, in this study, we train the model using physics-informed LSTM as it has shown very good potential in process modeling for Copper. The findings of PINN are also compared to the previous data-driven predictions.

The material of interest, Ti-7Al, can demonstrate slip and twin deformation behavior. Therefore, to run crystal plasticity simulations, the slip and twin parameters are defined as the input to the software. These parameters have possible ranges (shown in Table 1) that were previously obtained using the experimental true stress-strain curve data for compression in the preliminary studies of our group [13, 51].

Like the forward process modeling of Cu, we have used the same process simulator with the constitutive model developed by Sundararaghavan et al. [49] to generate the training data samples for a compression process. The crystal plasticity parameters are defined as the input and the ODFs are the output. A total of 50 random combinations of the slip and twin parameters are chosen within the given ranges in Table 1 to generate training data. Using this small dataset, another physics-informed surrogate model is trained using the LSTM network of Fig. 2. The combinations are split in 80%-10%-10% as training, validation, and test sets where the learning rate is set to 0.01. To prevent overfitting,

Table 2 Optimum slip and twin system parameters obtained from PINN-based inverse optimization that provide the best match with the experimental ODFs after compression

Slip System	s_0 (MPa)	h_0 (MPa)	s_s (MPa)	a
Basal $< a >$	324.5	297.9	1620.2	1.3
Prismatic $< a >$	225.7	295.1	1780.8	1.97
Pyramidal $< a >$	1170.9	216.8	1682.5	1.9
Pyramidal $< c + a >$	947.3	296.3	1629.7	2.0
Twinning	775.2	1101.9	1546.8	3.7

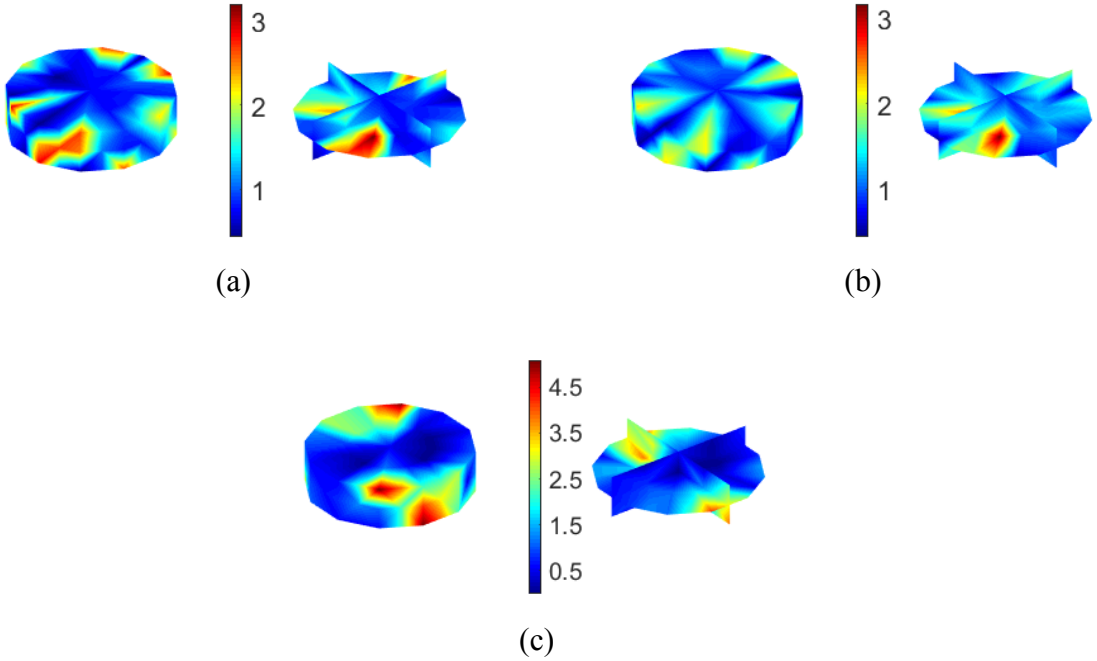

Fig. 7 ODFs in the Rodrigues orientation space (a) Experimental ODFs after compression, (b) ODFs predicted by PINN, and (c) ODFs predicted by a conventional neural network.

training is stopped early at the 900^{th} epoch along with a batch size of only 2. Unlike the first approach, in this case, the input layer has 20 features (slip and twin system parameters) and the output layer has 50 independent ODFs of Ti-7Al. Similar to the previous model, these ODFs need to satisfy the volume normalization constraint which is incorporated in the training by customizing the loss function (see Eq. 15).

Accuracy of the trained model in terms of comparison between the actual and predicted normalized ODFs, and mean squared error for training and validation data are reported in Fig. 5. The first test case shows a little discrepancy between the actual and predicted ODFs with an RMSE value of 0.27. However, the other two cases exhibit promising agreement between the actual and predicted ODFs with RMSE values of 0.03 and 0.05, respectively. Next, we estimate the optimum crystal plasticity parameters that provide the best match with the given experimental ODF values. The experimental ODF values, shown in Fig. 7, are derived from the Euler angles information using the closest simplex search technique to group the orientation information [54]. The EBSD images of the Ti-7Al sample are obtained at 13.5% compressive strain [53]. Figure 7a was taken after the end of the compression process and Fig. 7b was collected after re-crystallization of the microstructure. Next, an inverse optimization problem is defined to solve this problem. Therefore, the objective of this optimization problem is to minimize the RMSE between the computational and experimental ODFs.

For the first problem, we solved the optimum slip and twin system parameters (see Table 2) that can provide the

Table 3 Optimum slip and twin system parameters obtained from PINN-based inverse optimization that provide the best match with the experimental ODFs after re-crystallization

Slip System	s_0 (MPa)	h_0 (MPa)	s_s (MPa)	a
Basal $< a >$	204.8	213.5	1775.1	1.4
Prismatic $< a >$	238.7	245.4	1780.5	1.9
Pyramidal $< a >$	915.5	237.8	1783.5	1.3
Pyramidal $< c + a >$	806.6	251.5	1779.7	1.3
Twinning	937.1	812.7	1754.3	3.7

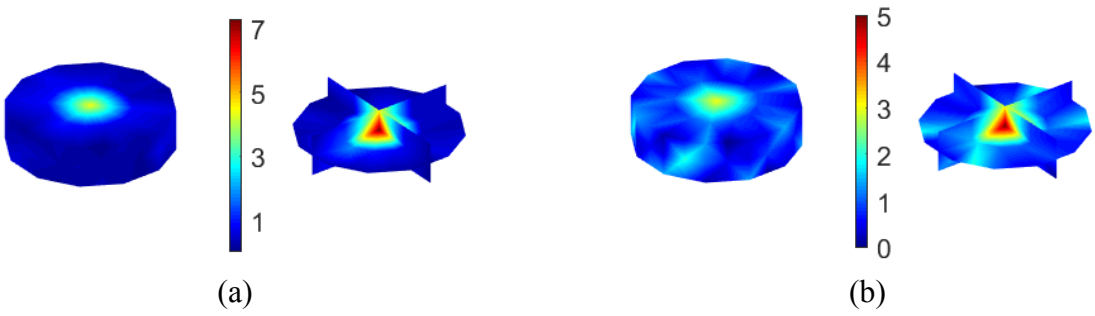

Fig. 8 ODFs in the Rodrigues orientation space (a) Experimental ODFs after re-crystallization and (b) ODFs predicted by PINN.

closest match of the optimum ODFs to the given experimental ODFs after compression. This problem was also solved by the conventional neural network before [13]. However, the prediction accuracy was found to be not sufficient. The RMSE value of the current prediction for all 50 ODFs is 0.41 which was 1.24 in the previous study (almost three times higher). Figure 7 reports the PINN-predicted ODFs in the Rodrigues orientation space along with the previous prediction by the conventional neural network, and the experimental ODFs for comparison. It is obvious that the physics-informed LSTM has improved the prediction accuracy compared to the conventional neural network with the incorporation of the problem physics.

Next, we calibrated the crystal plasticity parameters, shown in Table 3, using inverse design optimization that aimed to find the best-matching ODFs with the known experimental ODFs after re-crystallization of the deformed microstructure. Even though the temperature was not assigned as an independent design variable during the training of the surrogate model, the performance of the trained model was also assessed for the experimental texture data after re-crystallization. The optimum ODFs from the prediction and the experimental ODFs in the orientation space are displayed in Fig. 8. The physics-informed surrogate model also performs well in this case, however, the RMSE value of the prediction is 0.67, which is larger than the previous case. The incorporation of the temperature effect in the surrogate model is expected to decrease this error value and can be explored in the future. Though the surrogate model predictions are found to improve the prediction accuracy compared to the previous data-driven ML results, there are still errors potentially arising from (i) epistemic uncertainty associated with the crystal plasticity simulations and (ii) aleatoric uncertainty arising from the experimental measurements of the microstructural texture.

IV. Conclusions

This study presents the application of physics-informed neural networks in microstructure-sensitive materials design. The developed physics-informed LSTM network provides very good accuracy for predicting the texture evolution of Copper under the tensile deformation process with the lowest RMSE value of 0.16 for all 76 ODFs. In another problem, to identify the crystal plasticity parameters of Ti-7Al given the after-deformation experimental texture, PINN shows promising results for the crystal plasticity parameters calibration as its RMSE value is 3 times smaller than the RMSE value of the conventional neural network prediction. Therefore, this work has provided insight for future works that would involve the crystal plasticity modeling of metals by considering the uncertainty of the microstructures using a physics-informed neural network. The developed surrogate models are demonstrated to capture the microstructural texture evolution in different time steps of different deformation processes while accounting for the physics-derived design constraints of the orientation space. This methodology can further be extended in the future to predict the changes not only in the microstructural features but also in time-dependent material properties (e.g, stress/strain fields of microstructures) during the plastic deformation of metals.

Acknowledgments

The authors would like to thank Professor John Allison from the Materials Science and Engineering Department at the University of Michigan for providing experimental microstructure data of Ti-7Al alloy.

The authors also acknowledge the support from the Air Force Office of Scientific Research Young Investigator

Program under grant FA9550-21-1-0120 and from the National Science Foundation under award number 2053840.

References

[1] Acar, P., "Machine Learning Approach for Identification of Microstructure–Process Linkages," *AIAA Journal*, Vol. 57, No. 8, 2019, pp. 3608–3614. https://doi.org/10.2514/1.J058244.

[2] Allison, J., Backman, D., and Christodoulou, L., "Integrated computational materials engineering: a new paradigm for the global materials profession," *Jom*, Vol. 58, No. 11, 2006, pp. 25–27.

[3] Raissi, M., Perdikaris, P., and Karniadakis, G. E., "Physics-informed neural networks: A deep learning framework for solving forward and inverse problems involving nonlinear partial differential equations," *Journal of Computational physics*, Vol. 378, 2019, pp. 686–707.

[4] Mueller, T., Kusne, A. G., and Ramprasad, R., "Machine learning in materials science: Recent progress and emerging applications," *Reviews in Computational Chemistry*, Vol. 29, 2016, pp. 186–273. https://doi.org/10.1002/9781119148739.ch4.

[5] Warde, J., and DM, K., "Use of neural networks for alloy design," *ISIJ international*, Vol. 39, No. 10, 1999, pp. 1015–1019. https://doi.org/10.2355/isijinternational.39.1015.

[6] Liu, R., Kumar, A., Chen, Z., Agrawal, A., Sundararaghavan, V., and Choudhary, A., "A predictive machine learning approach for microstructure optimization and materials design," *Scientific reports*, Vol. 5, No. 1, 2015, pp. 1–12. https://doi.org/10.1038/srep11551.

[7] Agrawal, A., and Choudhary, A., "Perspective: Materials informatics and big data: Realization of the "fourth paradigm" of science in materials science," *Apl Materials*, Vol. 4, No. 5, 2016, p. 053208. https://doi.org/10.1063/1.4946894.

[8] Liu, Y., Zhao, T., Ju, W., and Shi, S., "Materials discovery and design using machine learning," *Journal of Materiomics*, Vol. 3, No. 3, 2017, pp. 159–177. https://doi.org/10.1016/j.jmat.2017.08.002.

[9] Kondo, R., Yamakawa, S., Masuoka, Y., Tajima, S., and Asahi, R., "Microstructure recognition using convolutional neural networks for prediction of ionic conductivity in ceramics," *Acta Materialia*, Vol. 141, 2017, pp. 29–38. https://doi.org/10.1016/j.actamat.2017.09.004.

[10] Paul, A., Acar, P., Liao, W.-k., Choudhary, A., Sundararaghavan, V., and Agrawal, A., "Microstructure optimization with constrained design objectives using machine learning-based feedback-aware data-generation," *Computational Materials Science*, Vol. 160, 2019, pp. 334–351. https://doi.org/10.1016/j.commatsci.2019.01.015.

[11] Acar, P., "Machine Learning Reinforced Crystal Plasticity Modeling under Experimental Uncertainty," *AIAA Scitech 2020 Forum*, 2020, p. 1152. https://doi.org/10.2514/6.2020-1152.

[12] Karniadakis, G. E., Kevrekidis, I. G., Lu, L., Perdikaris, P., Wang, S., and Yang, L., "Physics-informed machine learning," *Nature Reviews Physics*, Vol. 3, No. 6, 2021, pp. 422–440.

[13] Hasan, M. M., Senthilnathan, A., and Acar, P., "Machine Learning Reinforced Multi-Scale Modeling of Microstructures under Uncertainties," *AIAA Scitech 2021 Forum*, 2021, p. 1140.

[14] Lee, H., and Kang, I. S., "Neural algorithm for solving differential equations," *Journal of Computational Physics*, Vol. 91, No. 1, 1990, pp. 110–131.

[15] Lagaris, I. E., Likas, A., and Fotiadis, D. I., "Artificial neural networks for solving ordinary and partial differential equations," *IEEE transactions on neural networks*, Vol. 9, No. 5, 1998, pp. 987–1000.

[16] Lagaris, I. E., Likas, A. C., and Papageorgiou, D. G., "Neural-network methods for boundary value problems with irregular boundaries," *IEEE Transactions on Neural Networks*, Vol. 11, No. 5, 2000, pp. 1041–1049.

[17] Sirignano, J., and Spiliopoulos, K., "DGM: A deep learning algorithm for solving partial differential equations," *Journal of computational physics*, Vol. 375, 2018, pp. 1339–1364.

[18] Raissi, M., Perdikaris, P., and Karniadakis, G. E., "Physics informed deep learning (part i): Data-driven solutions of nonlinear partial differential equations," *arXiv preprint arXiv:1711.10561*, 2017.

[19] Raissi, M., Perdikaris, P., and Karniadakis, G. E., "Physics Informed Deep Learning (Part II): Data-driven Discovery of Nonlinear Partial Differential Equations," *CoRR*, Vol. abs/1711.10566, 2017. URL http://arxiv.org/abs/1711.10566.

[20] Haghighat, E., Raissi, M., Moure, A., Gomez, H., and Juanes, R., "A physics-informed deep learning framework for inversion and surrogate modeling in solid mechanics," *Computer Methods in Applied Mechanics and Engineering*, Vol. 379, 2021, p. 113741.

[21] Arora, R., "Machine learning-accelerated computational solid mechanics: Application to linear elasticity," *arXiv preprint arXiv:2112.08676*, 2021.

[22] Zhang, E., Dao, M., Karniadakis, G. E., and Suresh, S., "Analyses of internal structures and defects in materials using physics-informed neural networks," *Science advances*, Vol. 8, No. 7, 2022, p. eabk0644.

[23] Fuhg, J. N., van Wees, L., Obstalecki, M., Shade, P., Bouklas, N., and Kasemer, M., "Machine-learning convex and texture-dependent macroscopic yield from crystal plasticity simulations," *Materialia*, 2022, p. 101446.

[24] Arora, R., Kakkar, P., Dey, B., and Chakraborty, A., "Physics-informed neural networks for modeling rate-and temperature-dependent plasticity," *arXiv preprint arXiv:2201.08363*, 2022.

[25] Mao, Z., Jagtap, A. D., and Karniadakis, G. E., "Physics-informed neural networks for high-speed flows," *Computer Methods in Applied Mechanics and Engineering*, Vol. 360, 2020, p. 112789.

[26] Cai, S., Mao, Z., Wang, Z., Yin, M., and Karniadakis, G. E., "Physics-informed neural networks (PINNs) for fluid mechanics: A review," *Acta Mechanica Sinica*, 2022, pp. 1–12.

[27] Yang, X., Zafar, S., Wang, J.-X., and Xiao, H., "Predictive large-eddy-simulation wall modeling via physics-informed neural networks," *Physical Review Fluids*, Vol. 4, No. 3, 2019, p. 034602.

[28] Almajid, M. M., and Abu-Al-Saud, M. O., "Prediction of porous media fluid flow using physics informed neural networks," *Journal of Petroleum Science and Engineering*, Vol. 208, 2022, p. 109205.

[29] Wessels, H., Weißenfels, C., and Wriggers, P., "The neural particle method–an updated Lagrangian physics informed neural network for computational fluid dynamics," *Computer Methods in Applied Mechanics and Engineering*, Vol. 368, 2020, p. 113127.

[30] Cai, S., Wang, Z., Wang, S., Perdikaris, P., and Karniadakis, G. E., "Physics-informed neural networks for heat transfer problems," *Journal of Heat Transfer*, Vol. 143, No. 6, 2021.

[31] Chen, Y., Lu, L., Karniadakis, G. E., and Dal Negro, L., "Physics-informed neural networks for inverse problems in nano-optics and metamaterials," *Optics express*, Vol. 28, No. 8, 2020, pp. 11618–11633.

[32] Fang, Z., and Zhan, J., "Deep physical informed neural networks for metamaterial design," *IEEE Access*, Vol. 8, 2019, pp. 24506–24513.

[33] Shaier, S., Raissi, M., and Seshaiyer, P., "Data-driven approaches for predicting spread of infectious diseases through DINNs: Disease Informed Neural Networks," *arXiv preprint arXiv:2110.05445*, 2021.

[34] Goswami, S., Li, D. S., Rego, B. V., Latorre, M., Humphrey, J. D., and Karniadakis, G. E., "Neural operator learning of heterogeneous mechanobiological insults contributing to aortic aneurysms," *arXiv preprint arXiv:2205.03780*, 2022.

[35] Sahli Costabal, F., Yang, Y., Perdikaris, P., Hurtado, D. E., and Kuhl, E., "Physics-informed neural networks for cardiac activation mapping," *Frontiers in Physics*, Vol. 8, 2020, p. 42.

[36] Misyris, G. S., Venzke, A., and Chatzivasileiadis, S., "Physics-informed neural networks for power systems," *2020 IEEE Power & Energy Society General Meeting (PESGM)*, IEEE, 2020, pp. 1–5.

[37] Oszkinat, C., Luczak, S. E., and Rosen, I., "Uncertainty Quantification in Estimating Blood Alcohol Concentration From Transdermal Alcohol Level With Physics-Informed Neural Networks," *IEEE Transactions on Neural Networks and Learning Systems*, 2022.

[38] Lütjens, B., Crawford, C. H., Veillette, M., and Newman, D., "PCE-PINNs: Physics-Informed Neural Networks for Uncertainty Propagation in Ocean Modeling," *arXiv preprint arXiv:2105.02939*, 2021.

[39] Zhang, D., Lu, L., Guo, L., and Karniadakis, G. E., "Quantifying total uncertainty in physics-informed neural networks for solving forward and inverse stochastic problems," *Journal of Computational Physics*, Vol. 397, 2019, p. 108850.

[40] Dornheim, J., Morand, L., Zeitvogel, S., Iraki, T., Link, N., and Helm, D., "Deep reinforcement learning methods for structure-guided processing path optimization," *Journal of Intelligent Manufacturing*, Vol. 33, No. 1, 2022, pp. 333–352.

[41] Honarmandi, P., Attari, V., and Arroyave, R., "Accelerated materials design using batch Bayesian optimization: A case study for solving the inverse problem from materials microstructure to process specification," *Computational Materials Science*, Vol. 210, 2022, p. 111417.

[42] Zhang, R., Liu, Y., and Sun, H., "Physics-informed multi-LSTM networks for metamodeling of nonlinear structures," *Computer Methods in Applied Mechanics and Engineering*, Vol. 369, 2020, p. 113226.

[43] Alhajeri, M. S., Abdullah, F., Wu, Z., and Christofides, P. D., "Physics-informed machine learning modeling for predictive control using noisy data," *Chemical Engineering Research and Design*, Vol. 186, 2022, pp. 34–49.

[44] Pombo, D. V., Bacher, P., Ziras, C., Bindner, H. W., Spataru, S. V., and Sørensen, P. E., "Benchmarking physics-informed machine learning-based short term pv-power forecasting tools," *Energy Reports*, Vol. 8, 2022, pp. 6512–6520.

[45] Li, X., Chen, S., Zhang, J., Gao, J., and Bai, Y., "A Physics-Informed Deep Learning Paradigm for Transient Power Angle Stability Assessment," *IEEE Journal of Radio Frequency Identification*, 2022.

[46] Kumar, A., and Dawson, P., "Computational modeling of FCC deformation textures over Rodrigues' space," *Acta Materialia*, Vol. 48, No. 10, 2000, pp. 2719–2736. https://doi.org/10.1016/S1359-6454(00)00044-6.

[47] Sundararaghavan, V., and Zabaras, N., "On the synergy between texture classification and deformation process sequence selection for the control of texture-dependent properties," *Acta materialia*, Vol. 53, No. 4, 2005, pp. 1015–1027.

[48] Smagulova, K., and James, A. P., "Overview of long short-term memory neural networks," *Deep Learning Classifiers with Memristive Networks*, Springer, 2020, pp. 139–153.

[49] Sundararaghavan, V., and Zabaras, N., "Linear analysis of texture–property relationships using process-based representations of Rodrigues space," *Acta materialia*, Vol. 55, No. 5, 2007, pp. 1573–1587. https://doi.org/10.1016/j.actamat.2006.10.019.

[50] Chandriah, K. K., and Naraganahalli, R. V., "RNN/LSTM with modified Adam optimizer in deep learning approach for automobile spare parts demand forecasting," *Multimedia Tools and Applications*, Vol. 80, No. 17, 2021, pp. 26145–26159.

[51] Acar, P., "Machine learning reinforced crystal plasticity modeling under experimental uncertainty," *AIAA Journal*, Vol. 58, No. 8, 2020, pp. 3569–3576.

[52] Yaghoobi, M., Ganesan, S., Sundar, S., Lakshmanan, A., Rudraraju, S., Allison, J. E., and Sundararaghavan, V., "PRISMS-Plasticity: An open-source crystal plasticity finite element software," *Computational Materials Science*, Vol. 169, 2019, p. 109078.

[53] Trump, A. M., and Allison, J. E., "The Influence of Aluminum Concentration on Static Recrystallization in Alpha Titanium Alloys," *Proceedings of the 13th World Conference on Titanium*, Wiley Online Library, 2016, pp. 695–696.

[54] Acar, P., and Sundararaghavan, V., "Uncertainty quantification of microstructural properties due to experimental variations," *AIAA Journal*, Vol. 55, No. 8, 2017, pp. 2824–2832.